Design, Control and Performance of RiceWrist: A Force Feedback Wrist Exoskeleton for Rehabilitation and Training

Abhishek Gupta, Marcia K. O'Malley, Volkan Patoglu and Charles Burgar

The International Journal of Robotics Research 2008; 27; 233

DOI: 10.1177/0278364907084261

Abhishek Gupta
Marcia K. O'Malley
Department of Mechanical Engineering and Materials Science
Rice University, Houston, TX 77005, USA
{abhi,omalleym}@rice.edu

Volkan Patoglu
Faculty of Engineering and Natural Sciences
Sabancı University
Tuzla, İstanbul 34956, Turkey
vpatoglu@sabanciuniv.edu

Charles Burgar, MD
CTVHCS, Temple, TX 76504, USA
charles.burgar1@med.va.gov

Design, Control and Performance of *RiceWrist*: A Force Feedback Wrist Exoskeleton for Rehabilitation and Training

Abstract

This paper presents the design, control and performance of a high fidelity four degree-of-freedom wrist exoskeleton robot, RiceWrist, for training and rehabilitation. The RiceWrist is intended to provide kinesthetic feedback during the training of motor skills or rehabilitation of reaching movements. Motivation for such applications is based on findings that show robot-assisted physical therapy aids in the rehabilitation process following neurological injuries. The exoskeleton device accommodates forearm supination and pronation, wrist flexion and extension and radial and ulnar deviation in a compact parallel mechanism design with low friction, zero backlash and high stiffness. As compared to other exoskeleton devices, the RiceWrist allows easy measurement of human joint angles and independent kinesthetic feedback to individual human joints. In this paper, joint-space as well as task-space position controllers and an impedance-based force controller for the device are presented. The kinematic performance of the device is characterized in terms of its workspace, singularities, manipulability, backlash and backdrivability. The dynamic performance of RiceWrist is characterized in terms of motor torque output, joint friction, step responses, behavior under closed loop set-point and trajectory tracking control and display of virtual walls. The device is singularity-free, encompasses most of the natural workspace of the human joints and exhibits low friction, zero-backlash and high manipulability, which are kinematic properties that characterize a high-quality impedance display device. In addition, the device displays fast, accurate response under position control that matches human actuation bandwidth and the capability to display sufficiently hard contact with little coupling between controlled degrees-of-freedom.

KEY WORDS—rehabilitation robotics, medical robots and systems, mechanism design, haptics and haptic interfaces, physical human-robot interaction

1. Introduction

The ability to interact mechanically with virtual objects through incorporation of haptic feedback allows users to manipulate objects in the simulated or remote environment with ease when compared to a purely visual display. Added advantages of haptic simulators include increased repeatability, scalability, safety and control over environmental conditions. It is also possible to simulate additional physical forces, which may or may not be part of a natural environment, in order to convey information to the user. This makes a haptic display suitable for a variety of applications such as remote operation in hazardous environments, simulators for surgical training (Basdogan et al. 2001; Feygin et al. 2002; Carignan and Akin 2003) and rehabilitation research (Todorov et al. 1997; Prisco et al. 1998; Jack et al. 2001; Sveistrup 2004). Physical therapy utilizing the resistance offered to a user's motion during haptic interaction can be used for rehabilitation of impaired arm movements in patients. Furthermore, research has shown that augmented feedback presented in virtual environments accelerates the learning of motor tasks (Todorov et al. 1997).

In 2003, 700 000 persons in the United States suffered a cerebral vascular accident (CVA) or stroke, with the total num-

The International Journal of Robotics Research
Vol. 27, No. 2, February 2008, pp. 233–251
DOI: 10.1177/0278364907084261

Figures 2, 9–28 appear in color online: http://ijr.sagepub.com

ber of survivors estimated at 5.5 million. The total cost for rehabilitation and lost revenue in 2006 was 57.9 billion (Thom et al. 2006). Stroke commonly causes significant residual physical, cognitive and psychological impairment (Gresham 1990). As the geriatric population increases and more effective therapies for acute stroke management emerge, there will be more survivors living with disabilities. There has also been a trend toward more moderately affected survivors (Wolf et al. 1992), which has increased the demand for stroke rehabilitation in an era of health care cost containment. Persons with hemiparesis following stroke constitute the largest group of patients receiving rehabilitation services in this country. Efforts to prevent stroke must, therefore, be balanced with pragmatic efforts to prevent disability and maximize quality of life for stroke survivors. Current consensus regarding rehabilitation of patients with some voluntary control over movements of the paretic limb is that they be encouraged to use the limb in functional tasks and receive training directed toward improving strength and motor control, relearning sensorimotor relationships and improving functional performance (Gresham et al. 1997). Research efforts that improve the effectiveness of rehabilitative treatment of motor disability resulting from stroke are needed. With the dramatic reduction of inpatient rehabilitation length of stay following stroke, efficient and effective interventions have become critical.

1.1. Robotic Rehabilitation Systems

Interest in the rehabilitation applications for robots has been increasing (Erlandson 1992; Reinkensmeyer et al. 1996; Reinkensmeyer et al. 2000). Khalili and Zomlefer suggested that a two-joint robot system could be used for continuous passive motion and could be programmed to the particular needs of the patient (Khalili and Zomlefer 1988). Goodall et al. (1987) used two single degree-of-freedom (DOF) arms to stabilize sway in hemiparetic patients and suggested the level of assistance could be withdrawn to encourage patients to relearn to balance on their own. White et al. (1993) built a single DOF pneumatically-powered orthotic device for elbow flexion that could be used for continuous passive motion, to measure patient strength and to assist elbow flexion. Dirette and Hinojosa (1994) showed that a continuous passive motion (CPM) machine, when used regularly, can effectively reduce edema in the hands of flaccid hemiparetic patients. As described here, the majority of robotic rehabilitation systems to date have focused on the upper extremity, specifically the shoulder and/or elbow.

Prior work has studied the ability of the MIME (Mirror-Image Motion Enabler) device (Burgar et al. 2000) to assist limb movements and facilitate recovery of motor function in subjects with chronic hemiparesis due to stroke. MIME incorporates an industrial robot and operates in three unilateral modes and one bimanual mode. In unilateral operation, passive, active-assisted and guided movements against a resistance are possible. The bimanual mode enables the subject to practice bilateral, coordinated movements with rate and range under his or her control.

In the current version of MIME, subjects are seated in a wheelchair modified to improve seating support and reduce movements of the upper body. They can sit close to either the front or rear of an adjustable height table. A PUMA-560 robot is mounted beside the table. It is attached to a wrist-forearm orthosis (splint) via a six-axis force transducer, a pneumatic breakaway overload sensor set to 20 Nm torque, and a quick-release coupling mechanism. The subject's arm is strapped into the splint with the wrist in neutral position. Robot/forearm interaction force and torque measurements from the transducer are recorded and archived by a personal computer. The control program monitors these data and the motion of the robot in order to prevent potentially hazardous situations from occurring. Switches and mechanical stops are strategically placed to permit rapid de-activation of the robot, if necessary.

In an initial study with MIME including 28 subjects (two groups of 14) all had improved motor function as a result of therapy (Burgar et al. 2000). The robot group, compared to the control group, had larger improvements in the proximal movement portion of the Fugl-Meyer (FM) test after one month of treatment and also after two months of treatment. The robot group also had larger gains in strength and larger increases in reach extent after two months of treatment. At the six-month follow-up, the groups no longer differed in terms of the Fugl-Meyer test, however the robot group had larger improvements in the Functional Independence Measure (FIM).

Preliminary data from these ongoing clinical efficacy trials suggest that robot-aided therapy has therapeutic benefits. Improvements have been demonstrated in strength and in the FM assessment of motor function. Trends in the data suggest that the underlying mechanisms for these results may be increased strength, as well as more appropriate activation and inhibition of muscle groups.

The reader is referred to extensive reviews of robotic therapy for upper and lower extremity for a more complete discussion of the state of the field (Fasoli et al. 2004; Hogan and Krebs 2004; Riener et al. 2005; Reinkensmeyer et al. 2004; Stein 2004; O'Malley et al. 2006). The MIME studies together with the cited related work support the conclusions that robotic manipulation of an impaired limb may favorably affect recovery following a stroke. An important additional finding is that improvements in motor control are possible beyond six months following a stroke.

However, the improvements in motor control following robotic therapy for shoulder and elbow were found to be local with limited benefits to the forearm, wrist and fingers (Fasoli et al. 2003). In order for a patient to relearn a task, each limb segment associated with the task should be rehabilitated (Charles et al. 2005). The findings with shoulder and elbow rehabilitation motivate the extension of robotic-assisted rehabilitation distally for the upper extremity, so that forearm pronation-supination, wrist flexion-extension, radial-ulnar deviation and ultimately digital manipulation are enabled. Several devices have been presented in the literature to achieve at least a subset of these movements. For example, Charles et al. (2005) have developed an extension of the MIT-MANUS system to provide three rotational degrees-of-freedom for wrist rehabilitation. Hesse et al. (2003) have also extended the utility of their arm trainer to include wrist motion. In order to improve the applicability of the MIME system for full arm rehabilitation post stroke, the authors have developed the *RiceWrist*, a modification of the MAHI exoskeleton (Gupta and O'Malley 2006; Sledd and O'Malley 2006), which interfaces with MIME and provides a variety of interaction modes for the therapist to select for the patient.

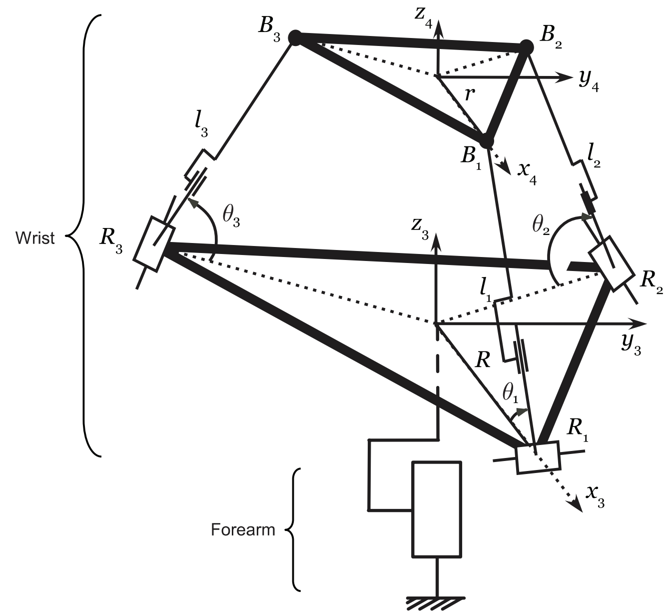

Fig. 1. *RiceWrist* mechanism: a 3-RPS platform is used as the wrist of the robot. Joints R_1, R_2 and R_3 and B_1, B_2 and B_3 are located at vertices of equilateral triangles.

2. Design of the *RiceWrist*

The *RiceWrist* is an electrically actuated forearm and wrist haptic exoskeleton device that has been designed for rehabilitation applications. The kinematic design of the *RiceWrist* allows for the reproduction of most of the natural human wrist and forearm workspace, force isotropy and high torque output levels required during robot-aided training and/or rehabilitation. Another important feature of the design is the alignment of the axes of rotation of human joints with the controlled degrees-of-freedom of the exoskeleton. The problem of measurement of arm position is thus reduced to the solution of the exoskeleton kinematics, with no further transformations required. This makes it possible to actuate the robot to control feedback to a specific human joint, for example to constrain the forearm rotation during wrist rehabilitation, without affecting other joints.

Robot-aided rehabilitation typically requires the use of virtual force fields for guidance or active assistance. The *RiceWrist* has high force output bandwidth, low backlash, low-friction, high backdrivability, high structural stiffness and a singularity free workspace, features characteristic of a high fidelity haptic interface. The forward and inverse kinematics of the robot can be solved uniquely at each point, thus making the measurement of arm position and force feedback to individual arm joints possible at high update rates.

The *RiceWrist* design extends from prior work by some of the authors. A thorough discussion of specific design considerations for the original MAHI exoskeleton and how each was addressed can be found in O'Malley (2006). The redesign of the MAHI exoskeleton, discussed by Sledd and O'Malley (2006), successfully addresses the limitations of the original device design. This paper discusses the design of the RiceWrist, and presents joint-space as well as task-space position controllers and an impedance-based force controller for the device.

The basic kinematic structure of the *RiceWrist* is depicted in Figure 1. The exoskeleton is comprised of a revolute joint at the forearm and a 3-RPS (revolute-prismatic-spherical) serial-in-parallel wrist. The 3-RPS platform, mentioned in Lee and Shah (1988), consists of a base plate, three extensible links l_1, l_2 and l_3 and a moving plate. The moving plate houses the end-effector that is affixed to the operator during operation. The moving plate is connected to the three extensible links by means of spherical joints spaced at 120° along the circumference of a circle of radius r. The other end of the links connects to the base plate via revolute (pin) joints, which are also spaced at 120° along a circle of radius R. The axes of rotation of the revolute joints are oriented along the tangents to this circle. Actuators placed along the link are used to change the link length, thereby moving the top plate. It should be noted that the platform has limited translational movement transverse to the vertical axis through the base and no singularities for $\theta_i \in (0, \pi)$ (Lee and Shah 1988). The device has four degrees-of-freedom corresponding to the rotation of the forearm, height of the wrist platform and two DOF in rotation of the top plate of the platform with respect to the base plate.

The choice of a parallel mechanism for the design of the *RiceWrist* over a serial mechanism was motivated primarily by the compactness of the parallel mechanism. Furthermore, use of a parallel mechanism allows for higher torque output, stiffness and decreased inertia as compared to a similar serial mechanism. The parameters of the platform were optimized to limit the size of the mechanism (Gupta and O'Malley 2006).

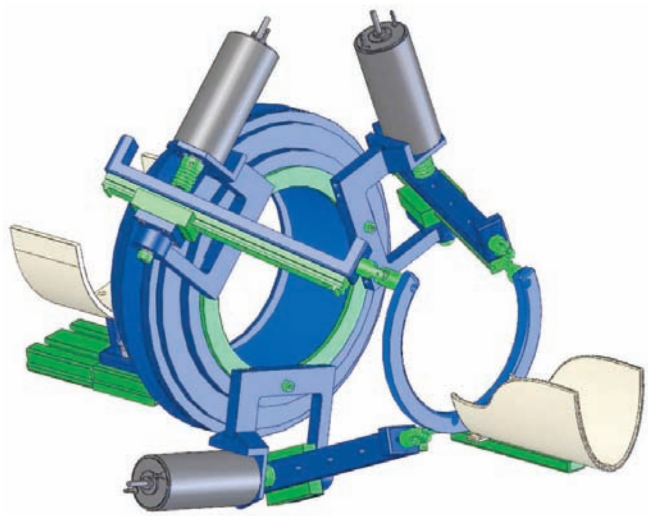

Fig. 2. Rendering of the mechanical design of the *RiceWrist*.

During operation, the robot is worn such that the top plate of the wrist of the robot aligns with the wrist joint of the operator. This configuration aids in preserving natural arm movements by aligning the robot's kinematic structure with that of the human arm. Velcro strapping and adjustable ergonomic upper forearm and palm splints are used to maintain the axes alignment. The mapping between the robot configuration and arm position is further simplified by the use of the 3-RPS kinematic structure for the robot.

2.1. Mechanical Design of the RiceWrist

Figure 2 depicts the 3-D rendering of the final design. The forearm joint employs a frameless brushless DC motor (Applimotion Inc., # 165-A-18) with direct actuation. Due to the use of frameless actuators, the amount of material required for construction was minimized thus keeping the weight of the device in check. The wrist platform is actuated through high torque rotary electric motors and a capstan drive transmission. Rotary actuators (Maxon Motors, #RE40) mounted on top of the base of the platform are used to implement the revolute joints whereas slides mounted on the motor shafts using a cable drive transmission serve as the prismatic joints. The range of motion of the spherical joint at the movable plate of the platform limits the workspace of platform. Equations developed by Lee and Shah (1988) were used to compute the range of rotations required from the spherical joint in order to meet our workspace criteria. It was found that commercially available spherical joints are not sufficient in meeting the workspace requirements. Hence, the spherical joint was replaced by a 4 DOF spherical joint between the top plate of the platform and the corresponding linear joint links. This joint consisted of a universal-joint attached at either end to the link and the moving platform via rotary joints. This adds redundancy to the system and permits larger rotations. For the purpose of kinematic analysis, the redundancy does not affect any of the geometric relations or equations. Mechanical stops at workspace limits, soft software stops and a emergency stop switch are employed to ensure operator safety. For a detailed discussion of the design of the mechanism the reader is referred to Gupta and O'Malley (2006) and Sledd and O'Malley (2006).

2.2. Wrist Kinematics

For the purpose of analysis, the coordinate axes are fixed to various joints of the exoskeleton, as shown in Figure 1. Frames $\{3\}$ and $\{4\}$ are fixed to the bottom and top plates of the platform, respectively.

Now, given the transformation matrix between frames $\{3\}$ and $\{4\}$, the position and orientation of the wrist platform can be computed, which provides the position and orientation of the human wrist. The equivalence between the human wrist joint angles and the xyz Euler angle representation for the orientation of the platform is shown in the following subsection.

As shown in Figure 1, the base coordinate frame $\{3\}$ is attached to the center of the base platform with the z_3 axis pointing vertically upwards and x_3 axis towards the first revolute joint, R_1. Frame $\{4\}$ is attached to the moving platform with the z_4 axis being normal to the platform and the x_4 axis pointing towards the first spherical joint, B_1. Using Grashof's criterion, it can be shown that the system has three degrees of freedom. Furthermore, due to the constraint imposed by the revolute joints, the rotation of the platform about axis z_4 is not possible. Hence, the platform has only two degrees-of-freedom in orientation and one in translation. The length of individual links are denoted by l_i. The homogeneous transformation matrix ${}^4T_3$, which represents $\{4\}$ in terms of the base frame, $\{3\}$ is

$$
{}^3T_4 = \begin{bmatrix} n_1 & o_1 & a_1 & x_c \\ n_2 & o_2 & a_2 & y_c \\ n_3 & o_3 & a_3 & z_c \\ 0 & 0 & 0 & 1 \end{bmatrix} \tag{1}
$$

where $(x_c, y_c, z_c)^T$ denotes the position of the origin of frame $\{4\}$ in the base frame. The direction cosines of the unit vectors x, y and z in the base frame are represented by $(n_1, n_2, n_3)^T$, $(o_1, o_2, o_3)^T$, and $(a_1, a_2, a_3)^T$. For subsequent analysis, all coordinates and lengths have been normalized using the base radius, R. The following are defined:

$$
\rho = \frac{r}{R}, \ L_i = \frac{l_i}{R} \tag{2}
$$

then

$$X_c = \frac{x_c}{R},\ Y_c = \frac{y_c}{R},\ Z_c = \frac{z_c}{R}. \tag{3}$$

2.2.1. Forward Kinematics

The forward kinematics for the platform involves solving simultaneous equations for the position and orientation of the movable platform in terms of the given link lengths. The fact that the manipulator is essentially a structure for fixed lengths has been used to derive these equations. If θ_i is the angle between link $R_i B_i$ and the base, then the coordinates of the spherical joints with respect to the base frame are

$$\begin{aligned} {}^3B_1 &= \begin{bmatrix} 1 - L_1 \cos\theta_1 \\ 0 \\ L_1 \sin(\theta_1) \end{bmatrix}, \\ {}^3B_2 &= \begin{bmatrix} \frac{-1}{2}(1 - L_2 \cos\theta_2) \\ \frac{\sqrt{3}}{2}(1 - L_2 \cos\theta_2) \\ L_2 \sin(\theta_2) \end{bmatrix}, \\ {}^3B_3 &= \begin{bmatrix} \frac{-1}{2}(1 - L_3 \cos\theta_3) \\ \frac{-\sqrt{3}}{2}(1 - L_3 \cos\theta_3) \\ L_3 \sin(\theta_3) \end{bmatrix}. \end{aligned} \tag{4}$$

The distance between any two spherical joints, $\sqrt{3}\, r$, can be used to implicitly relate θ_i to L_i. This leads to three constraint equations given as

$$\begin{aligned} & L_1^2 + L_2^2 - 3 - 3\rho^2 + L_1 L_2 \cos\theta_1 \cos\theta_2 \\ - & 2L_1 L_2 \sin\theta_1 \sin\theta_2 - 3L_1 \cos\theta_1 - 3L_2 \cos\theta_2 = 0, \quad (5) \\ & L_3^2 + L_2^2 - 3 - 3\rho^2 + L_3 L_2 \cos\theta_3 \cos\theta_2 \\ - & 2L_3 L_2 \sin\theta_3 \sin\theta_2 - 3L_3 \cos\theta_3 - 3L_2 \cos\theta_2 = 0, \quad (6) \\ & L_1^2 + L_3^2 - 3 - 3\rho^2 + L_1 L_3 \cos\theta_1 \cos\theta_3 \\ - & 2L_1 L_3 \sin\theta_1 \sin\theta_3 - 3L_1 \cos\theta_1 - 3L_3 \cos\theta_3 = 0. \quad (7) \end{aligned}$$

Multiple solutions of θ_1, θ_2 and θ_3 for a given set of link lengths are possible. A further mathematical constraint

$$0^\circ < \theta_i < 180^\circ$$

ensures uniqueness. In other words, position z_c for the platform must always be positive, i.e. the moving platform should always move on one side of the base platform: a physical constraint. With this constraint, equations (5)–(7) can be solved numerically for θ_i.

As the spherical joints are placed at the vertices of an equilateral triangle, the Cartesian position of the origin of the moving frame {4}, which is the centroid of the triangle, can be calculated.

The Cartesian position of the spherical joints can be expressed as

$$\begin{bmatrix} {}^4B_i \\ 1 \end{bmatrix} = {}^4T_3 \begin{bmatrix} {}^3B_i \\ 1 \end{bmatrix}. \tag{8}$$

Equations (8) and (4) can be solved to determine the vectors **n**, **o** and **a** and hence the orientation of the platform. Once the transformation matrix T is known, the orientation of the platform in terms of xyz-Euler angles, α, β and γ, can be determined using

$$\begin{aligned} \beta &= \sin^{-1}(n_3),\ \alpha = \operatorname{atan2}\left(\frac{-o_3}{\cos(\beta)}, \frac{a_3}{\cos(\beta)}\right), \\ \gamma &= \operatorname{atan2}\left(\frac{-n_2}{\cos(\beta)}, \frac{n_1}{\cos(\beta)}\right). \end{aligned}$$

It should be noted that if $\beta = \pm 90^\circ$, α and γ become indeterminate. In addition, the top plate of the platform cannot rotate about z_4 and hence $\gamma = 0$ in general. For a detailed discussion of forward kinematics, refer to Gupta and O'Malley (2006).

2.2.2. Inverse Kinematics

As the moving platform has three degrees-of-freedom, its position can be defined in terms of the first two xyz-Euler angles, α and β, and one Cartesian coordinate, Z_c. As the links R_1B_1, R_2B_2 and R_3B_3 are constrained by the revolute joints to move in the planes $y = 0$, $y = -\sqrt{3}$ and $y = \sqrt{3}x$, respectively, using equation (8) we have

$$n_2\rho + Y_c = 0,\ X_c = \frac{\rho}{n_1 - o_2}.$$

Now, $\gamma = 0$ as the top plate of the platform cannot rotate about z_4. Hence, X_c, Y_c and γ can be easily solved. The orientation and position of the top plate can then be used to compute the transformation matrix T and determine the Cartesian positions B_i using equation (8). The actuator position is then trivial to calculate as the length of link $R_i B_i$.

2.2.3. Measurement of Human Wrist Joint Angles

A simplified kinematic model of the human lower arm and the wrist is shown in Figure 3. Notice that axes x_4 of the plat-

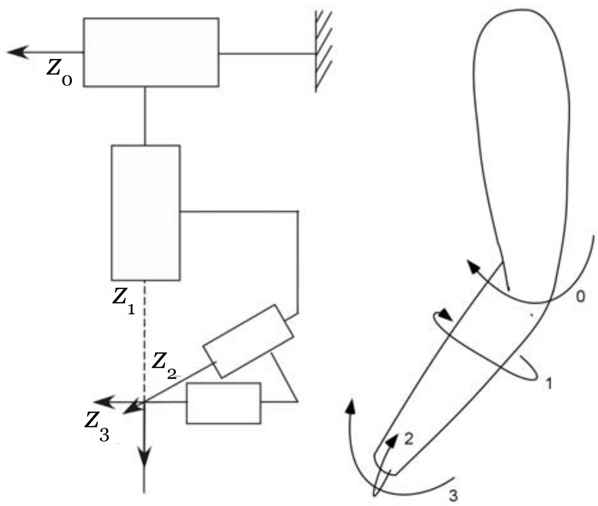

Fig. 3. Simplified kinematic model of the human arm. Other axes have not been shown for clarity. Axes 0–3 represent elbow rotation, forearm rotation, wrist adduction/abduction and wrist flexion/extension, respectively.

form (see Figure 1) and z_2 of the human wrist joint coincide when the exoskeleton is worn by an operator. Similarly, axes y_4 of the platform and z_3 of the arm coincide for any rotation α of the top plate of the platform about x_4, or of the human wrist about z_2 (Figure 3). Furthermore, $\{3\}$ of the platform has a fixed orientation with respect to $\{1\}$ of the human arm. Hence, a rotation of the top plate of the platform about axis x_4 (Figure 1) followed by another rotation about axis y_4 (Figure 1), is equivalent to a transformation from $\{3\}$ to $\{1\}$ of the arm. This implies that with the top plate of the platform centered at the operator's wrist joint, the Euler angle of rotation α about axis x_4 corresponds to abduction/adduction of the wrist while the rotation angle β about y_4 corresponds to flexion/extension.

2.3. Jacobian for the Wrist Platform

This section presents the derivation of the Jacobian of the wrist platform. The Jacobian relates the actuated linear degrees-of-freedom of the wrist to the task-space of the wrist. Note that for the purpose of this work the task-space is considered to be the flexion/extension, abduction/adduction and height of the platform. As described in the previous section, the abduction/adduction and flexion/extension of the the wrist correspond to the xyz-Euler angles of orientation of the top plate. The components of the transformation matrix ${}^3T_4$ relating the top and bottom plates are given by:

$$
\begin{aligned}
n_1 &= \cos\beta, \quad n_2 = 0, \quad n3 = \sin\beta, \\
o_1 &= \sin\alpha\sin\beta, \quad o_2 = \cos\alpha, \quad o_3 = -\cos\beta\sin\alpha, \\
a_1 &= -\sin\beta\cos\alpha, \quad \alpha a_2 = \sin\alpha, \quad a_3 = \cos\beta, \\
X_c &= \rho(n_1 - o_2)/2, \quad Y_c = -\rho n_2, \quad Z_c = z,
\end{aligned}
$$

where α and β are the wrist abduction/adduction and flexion/extension angles, and z is the height of the platform. The link lengths for the wrist platform are then given by:

$$
\begin{aligned}
L_1^2 &= (n_1\rho + X_c - 1)^2 + (n_2\rho + Y_c)^2 \\
&+ (n_3\rho + Z_c)^2, \qquad (9) \\
L_2^2 &= ((-n_1\rho + \sqrt{3}o_1\rho + 2X_c + 1)^2 \\
&+ (-n_2\rho + \sqrt{3}o_2\rho + 2Y_c - \sqrt{3})^2 \\
&+ (-n_3\rho + \sqrt{3}o_3\rho + 2Z_c)^2)/4, \qquad (10) \\
L_3^2 &= ((-n_1\rho - \sqrt{3}o_1\rho + 2X_c + 1)^2 \\
&+ (-n_2\rho - \sqrt{3}o_2\rho + 2Y_c + \sqrt{3})^2 \\
&+ (-n_3\rho - \sqrt{3}o_3\rho + 2 \times Z_c)^2)/4. \qquad (11)
\end{aligned}
$$

Differentiating equations (9)–(11) with respect to $[\alpha\ \beta\ Z_c]^T$ yields the device Jacobian.

3. Control of the *RiceWrist*

The *RiceWrist* is controlled via a 3.2 GHz Pentium 4 PC with 2 GB of RAM. To free up processor time, a 128 MB graphics card (AGP) was selected. The hardware is controlled through the MatLab Real Time Workshop Toolbox from Mathworks, and WinCon from Quanser Consulting. All data I/O is handled by the Quanser Q8 board, designed specifically for hardware in loop applications. Position and force controllers were designed for both the forearm and the wrist platform. Separate joint-space and task-space controllers were designed and tested for the wrist platform. Note that the task-space of the wrist platform refers to the two degrees-of-freedom corresponding to flexion/extension and abduction/adduction of the wrist and the height of the platform. The following sections describe controller design in detail.

3.1. Joint Space Position Control

Joint level control for the *RiceWrist* is implemented via a joint-space proportional derivative (PD) trajectory controller, as shown in Figure 4. In addition, an inverse kinematics based task-space position controller was designed for the wrist, as

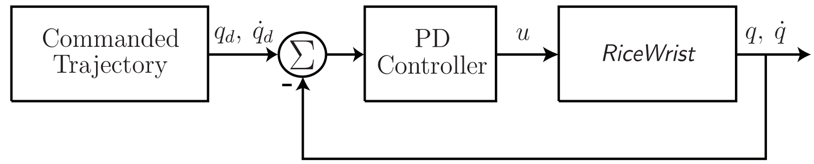

Fig. 4. Joint level PD trajectory controller for the *RiceWrist* system, where $q_\mathrm{d}, \dot{q}_\mathrm{d}$ are the desired joint position and velocities, $q, \dot{q}$ are the current joint position and velocities and u is the control input.

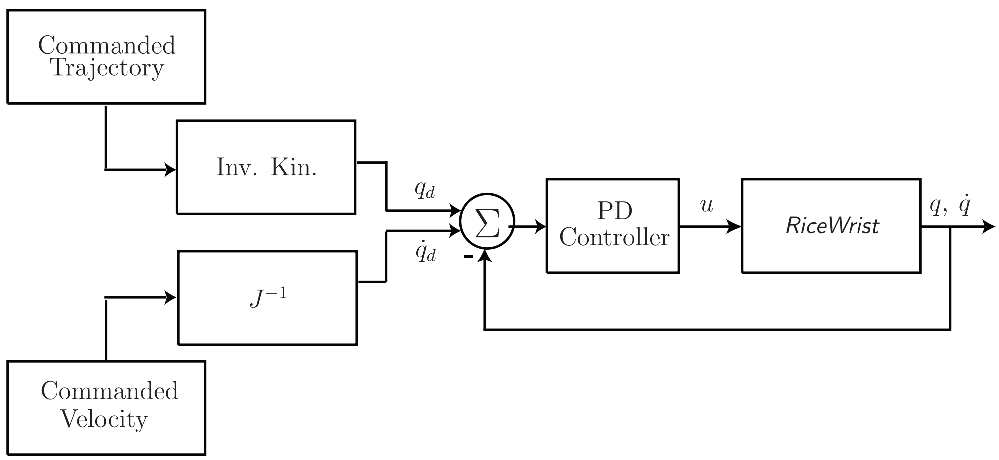

Fig. 5. Inverse kinematics-based trajectory controller for the *RiceWrist*, where J is the Jacobian of the device $q_\mathrm{d}, \dot{q}_\mathrm{d}$ are the desired joint position and velocities, $q, \dot{q}$ are the current joint position and velocities and u is the control input.

shown in Figure 5. The commanded task-space positions and velocities were used to generate reference commands for the aforementioned joint-space controller. The performance of the device under joint-space position control was verified through step responses, set point control and trajectory following control as described in Section 4.2.

3.2. Task-Space Position Control of the Wrist Platform

A task-space PD position controller for the wrist platform was also implemented as shown in Figure 6. As compared to the inverse kinematics based controller described in the previous section, this controller allows for independent control of wrist degrees-of-freedom, namely abduction/adduction, flexion/extension and platform height. This is critical as during operation it is desirable to constrain the height of the platform to be a constant dependent upon the length of the subject's forearm. Furthermore, this provides the ability to selectively provide guidance and/or feedback to individual human wrist joints. Step response, set-point control and trajectory following behavior of the controller are discussed in Section 4.2.

3.3. Force Control

Force control for the *RiceWrist* is implemented as a task-space impedance force controller, as shown in Figure 7. It is assumed that the accelerations and velocities associated with the motion are small enough to ignore the dynamic terms in the equations of motion of the device. It should be noted that in the case of the forearm, the task-space and the joint-space are the same and hence the impedance controller is simply a joint-space controller. The results of force control are discussed in Section 4.2 through haptic display of virtual walls.

4. Performance of the *RiceWrist*

4.1. Kinematic Performance

Table 1 shows the workspace for the *RiceWrist* in terms of the range of motion about each of the three primary degrees-of-freedom and corresponding human joint workspace limits. The singularity-free workspace of the *RiceWrist* is 100% of the average human joint range of motion except for palmar flexion and dorsiflexion where it is 60%. As shown in Figure 8, compound movements of the wrist remain singularity-free, albeit

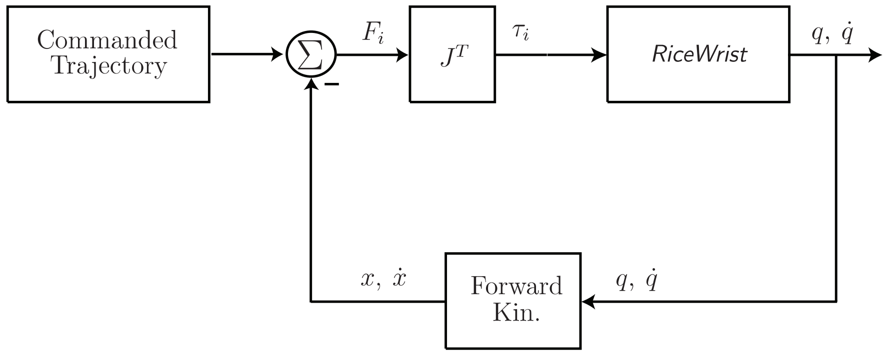

Fig. 6. Task-space PD position controller for the wrist platform, where $q, \dot{q}$ are the current joint position and velocities, $x, \dot{x}$ are the current task-space position and velocities, F_i is the desired environment force, J is the Jacobian of the *RiceWrist* and τ_i is the desired joint torque.

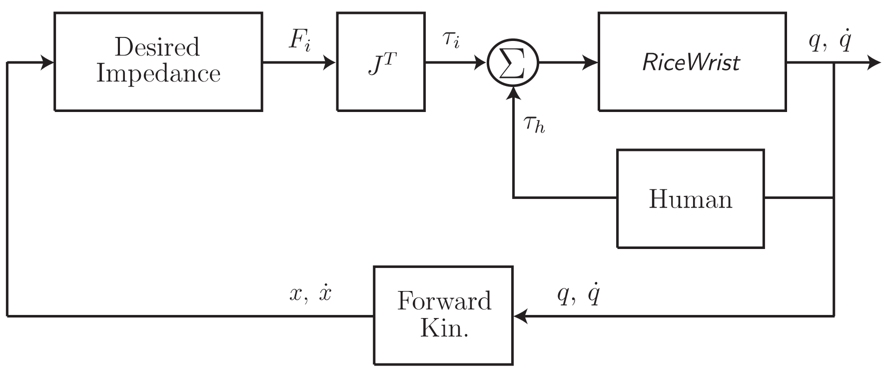

Fig. 7. Task-space impedance controller for the *RiceWrist* system, where $q, \dot{q}$ are the current joint position and velocities, $x, \dot{x}$ are the current task-space position and velocities, F_i is the desired environment force, J is the Jacobian of the *RiceWrist*, τ_i is the desired joint torques and τ_h is the human-induced joint torque.

Table 1. Comparison of workspace and torque limits of human arm and joints.

Joint	Human isometric strength[a]	Human joint workspace limits	Peak torque output capability	Workspace capability
Forearm Supination/Pronation	9.1 Nm	Supination: 86° Pronation: 71°	5.08 Nm	Supination: 90° Pronation: 90°
Wrist Palmar/Dorsal Flexion	19.8 Nm	Palmar Flexion: 73° Dorsiflexion: 71°	$\approx$ 5.3 Nm	Palmar Flexion: 42° Dorsiflexion: 42°
Wrist Abduction/Adduction	20.8 Nm	Adduction: 33° Abduction: 19°	$\approx$ 5.3 Nm	Adduction: $>$ 33° Abduction: $>$ 19°

[a]Source: Tsagarakis et al. 1999

with some reduction in the range of motion similar to the case of a human wrist. Thus the *RiceWrist* provides adequate range of motion for a human operator. It should also be noted that the device is backlash-free due to the use of direct drive and capstan-driven actuation and is highly backdrivable. Furthermore, the 3-RPS platform allows for compact design, centered

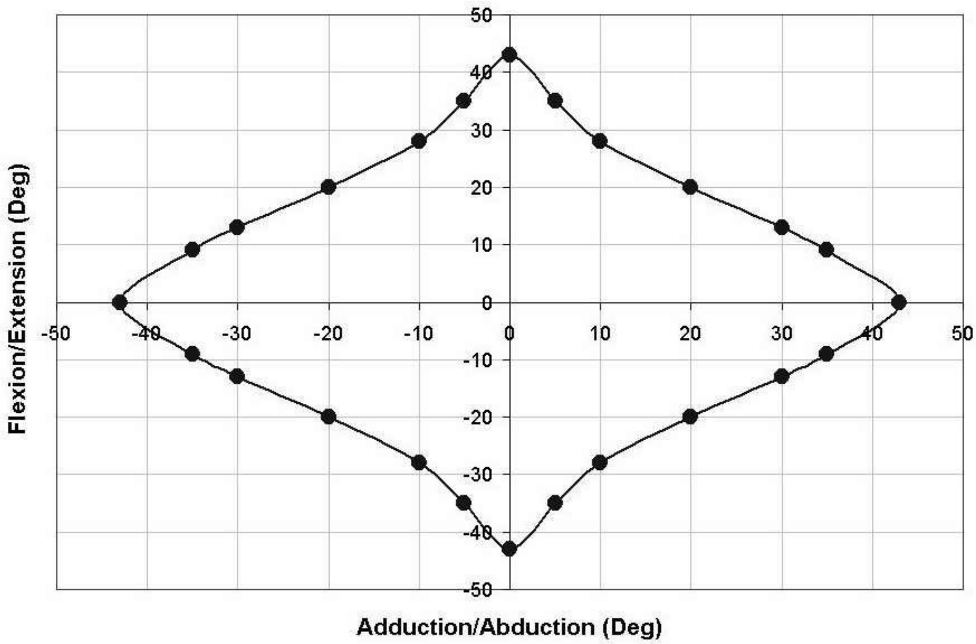

Fig. 8. Range of motion for the *RiceWrist*.

on the human arm, which increases wearability and maximizes the achievable workspace of the exoskeleton.

Figure 9(a) shows the manipulability of the *RiceWrist* measured as the absolute determinant of the inverse Jacobian (Yoshikawa 1985). Manipulability of a robot is a quantitative measure that captures the ease with which the device can arbitrarily change position and orientation from a given posture. For the *RiceWrist*, the manipulability measure is greatest in the center of the workspace, with the wrist at 0° of abduction/adduction (α) and flexion/extension (β). Manipulability, as expected, is low at the extents of each joint range of motion, more so during flexion/extension. For the tasks of rehabilitation and training, it is expected that the most useful interactions via the haptic device will take place away from the joint limits, and so manipulability should not limit device performance. The inverse of the condition number ($\|J^{-1}\|\|J\|$) is depicted in Figure 9(b). Again note that this has the highest value at the center of the device workspace and decreases on moving towards joint limits.

4.2. Dynamic Performance

Several performance measures have been proposed in the literature for the characterization of dynamic performance of haptic interfaces. These performance measures include peak force, peak acceleration, inertia and stiffness at the device/body interface (Hayward and Astley 1996). These measures are typically used for devices that provide single point haptic interaction, for example the PHANToM haptic interface by Sensable Technologies. For devices with multiple device/body interfaces such as the *RiceWrist*, however, measurements at the endpoint are not directly applicable. Hence, only data related to specific joints are provided. The total weight of the *RiceWrist* is 1.96 kg, comprising: forearm motor (stator + rotor) of 0.73 kg, wrist electrical motors (combined) of 0.65 kg and movable wrist components of 0.58 kg.

Table 1 lists the human isometric strength and the peak torque output capabilities of the *RiceWrist* for the corresponding joints. The torque capabilities lag behind human abilities due to practical considerations owing to the power-to-weight characteristics of electrical actuators. Coulomb friction was measured to be 0.041 Nm and 1.134 Nm in the forearm and wrist joints, respectively. Viscous friction was found to be negligible. The structural stiffness of the device is not of concern as the choice of a parallel mechanism ensures higher stiffness as compared to similarly sized serial interfaces. Note that the final stiffness is determined by the compliance introduced by the cable drives. Following sections present the closed loop performance results for the *RiceWrist*. Some of these results are also discussed in Gupta and O'Malley (2007).

4.2.1. Dynamic Performance of the Forearm

Position Control. As described in Section 3.1, the position control for the forearm was implemented through a PD controller.

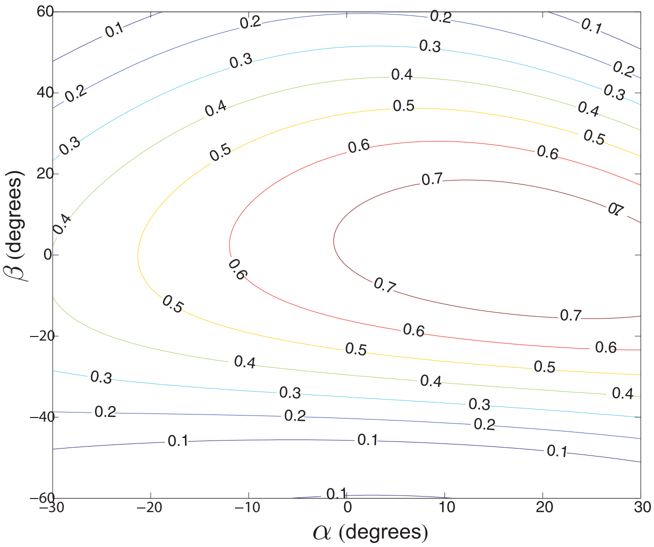

(a) Manipulability

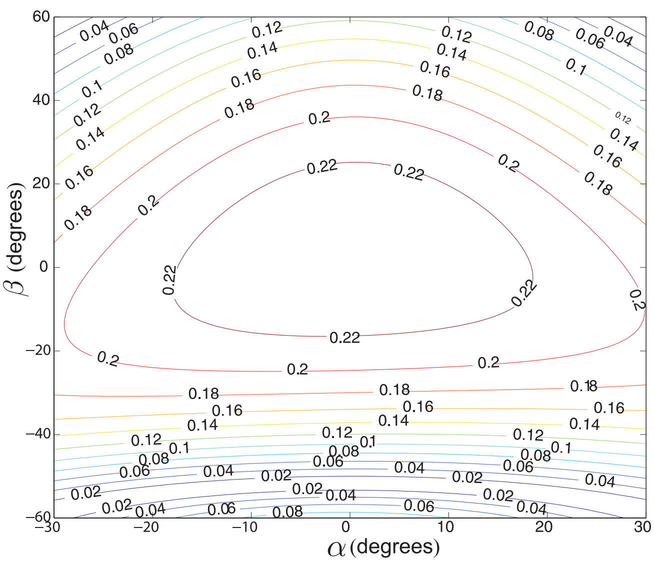

(b) $\frac{1}{\mathrm{ConditionNumber}}$

Fig. 9. (a) Manipulability of the wrist mechanism and (b) Condition Number^{-1}, where α is abduction/adduction and β is flexion/extension.

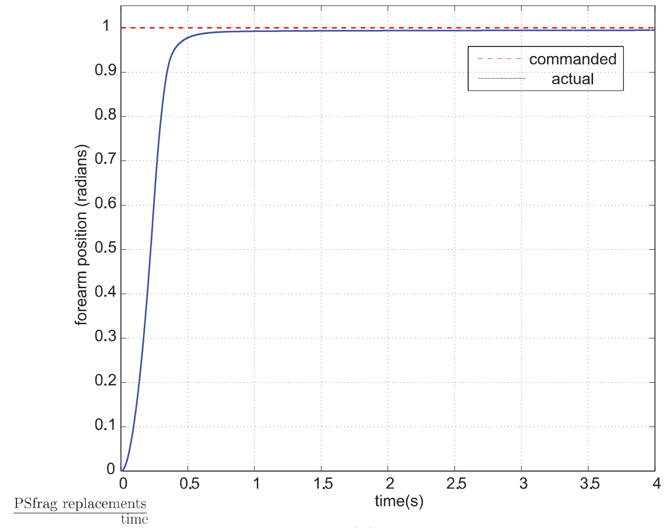

(a)

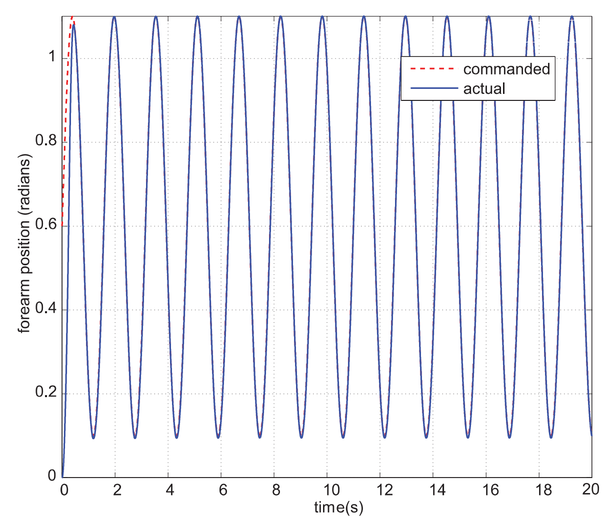

(b)

Fig. 10. Position control of the forearm position controller: (a) step response to a reference signal with a step of 1 rad shows no overshoot and quick, non-oscillatory response. (b) trajectory following behavior when tracking a 4 rad s^{-1} sinusoidal reference signal of amplitude 0.5 rad centered at 0.6 rad demonstrates that the device bandwidth matches human capabilities.

Figure 10(a) shows the closed loop step response of the forearm. It can be easily seen that the device reaches a steady-state position of 1 rad in less than 1 s with no overshoot or oscillations. There is a small steady-state error ($< 1\%$) in position due to friction in the bearings, motor cogging and the gravitational torque acting on the joint. The steady-state error can be eliminated with the use of a PID controller instead of the employed PD controller. The trajectory following behavior of the forearm tracking a sinusoidal reference signal at a frequency of 4 rad s^{-1} is depicted in Figure 10(b). This further verifies that the bandwidth of the controller is over 4 rad s^{-1} and matches human actuation bandwidth.

Force Control. As described in Section 3.3, force control for the forearm was implemented through an impedance controller. Figure 11 depicts a subject's interaction with a virtual wall, implemented as a spring-mass system of stiffness 150 Nm rad^{-1} and damping of 10 Nm rad^{-1} s^{-1}, located at 1 rad. Regions (a), (b) and (c) demonstrate the approach,

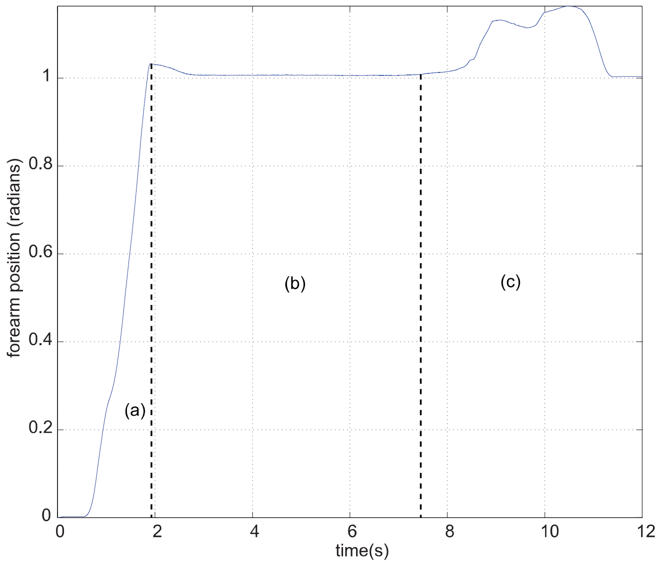

Fig. 11. User interaction with virtual wall located at 1 rad for the forearm joint. Regions (a), (b) and (c) demonstrate the approach, steady contact and penetration into the wall.

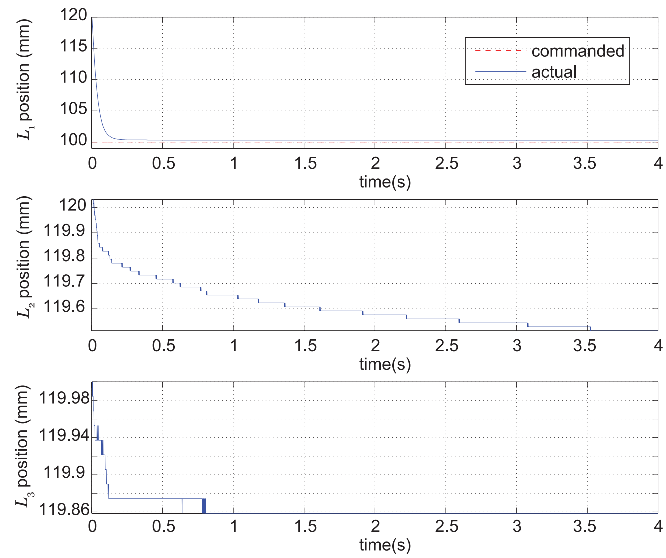

Fig. 12. Typical step response of wrist joint axis under PD control to a step of amplitude 80 mm (axis L1). Note that the system reaches steady state in less than 0.5 s with no overshoot. Small deviation of the non-actuated joints from their nominal position demonstrates low structural coupling between the axes.

steady contact and penetration into the wall, respectively. Note that due to torque limitations of the forearm motor, the user can overcome the wall force, thereby saturating the motor. Larger motor output is desired for simulating stronger walls, but device torques that exceed human limits could compromise user safety.

4.2.2. *Dynamic Performance of the Wrist*

Joint Space Position Control. Joint level position control for the wrist was implemented via independent PD controllers acting on each joint, as discussed in Section 3.1. Figure 12 shows the response of one of the three linear joint axes to a step input with a step of 80 mm. Other axes had a similar response. Note that the three axes were not actuated simultaneously. The controlled joint axis shows a non-oscillatory convergence to the steady state in less than 0.5 s without any overshoot. The small steady-state error ($< 1\%$) is due to frictional effects and the stiffness of the cable transmission and can be eliminated with the use of a PID controller. Note that the non-actuated joints show a maximum deviation of 0.5 mm from their initial position. This demonstrates that there is negligible structural coupling between the actuated joints. The low structural coupling between the linear joint axes also serves to verify the mechanical design process showing that the axes could be independently controlled as theoretically predicted.

Figures 13 and 14 depict the performance of the wrist under joint level set-point and trajectory following control. The reference signals for the set-point and trajectory tracking were steps of amplitudes 100 mm, 90 mm and 80 mm, and sinusoidal signals of an amplitude of 1 cm at 2 rad s^{-1}. These results fur-

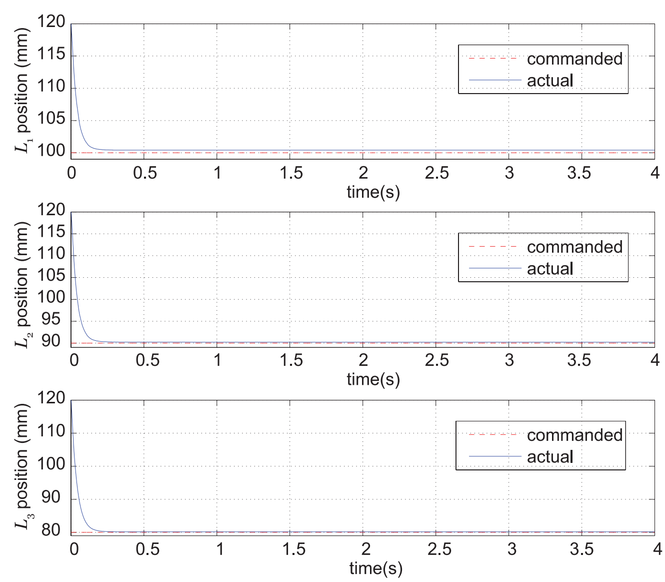

Fig. 13. Set point control of wrist joint axes using PD control with reference amplitudes of 100 mm, 90 mm and 80 mm. Note the quick convergence to steady state in < 0.5 s and low steady-state error ($< 1\%$).

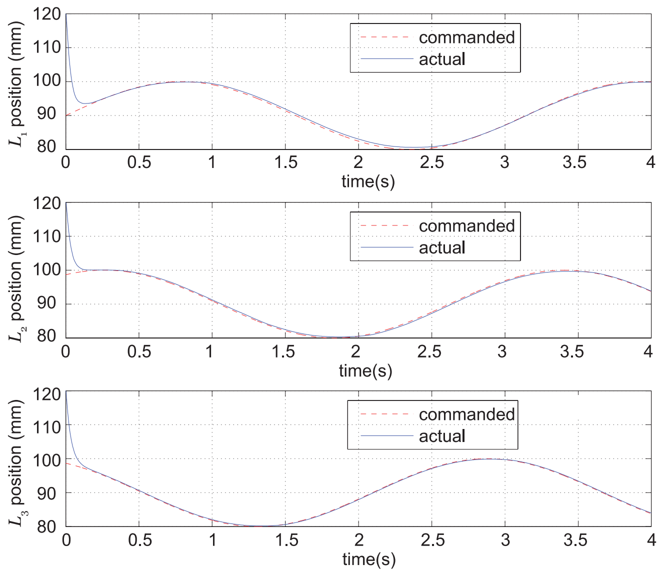

Fig. 14. Trajectory following behavior of the wrist joint axes under PD control. The reference signals are sinusoids with an amplitude of 1 cm and a frequency of $2\,\mathrm{rad\,s^{-1}}$. The actuator bandwidth matches human capabilities.

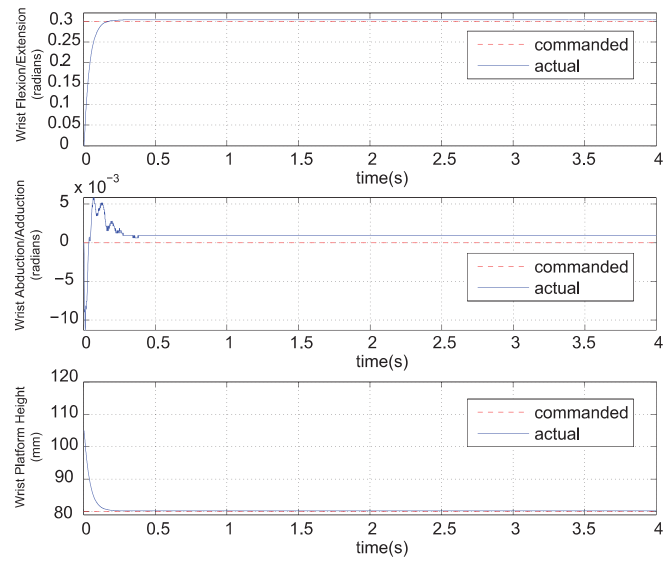

Fig. 16. Set point control of wrist flexion/extension using inverse kinematics and joint-level PD control (height: 80 mm; abduction/adduction: 0 rad; flexion/extension: 0.3 rad). Note the fast response time (< 0.5 s) and small steady-state error.

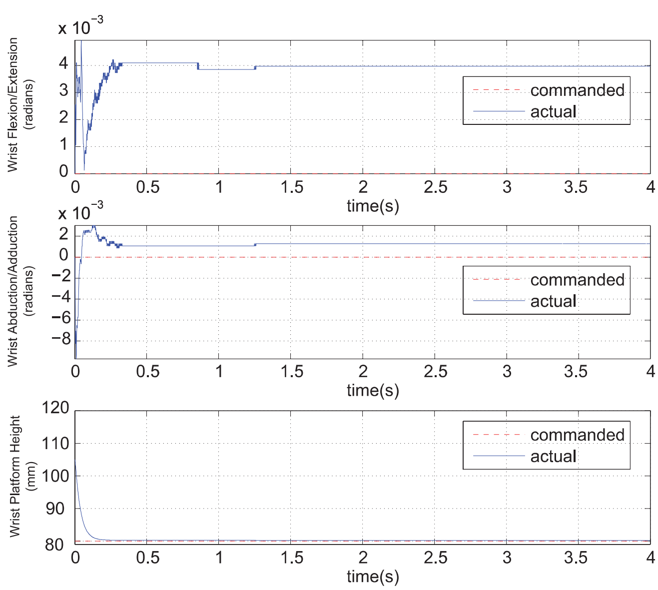

Fig. 15. Set point control of platform height using inverse kinematics and joint-level PD control (height: 80 mm; abduction/adduction: 0 rad; flexion/extension: 0 rad). Note the fast response time (< 0.5 s) and small steady-state error.

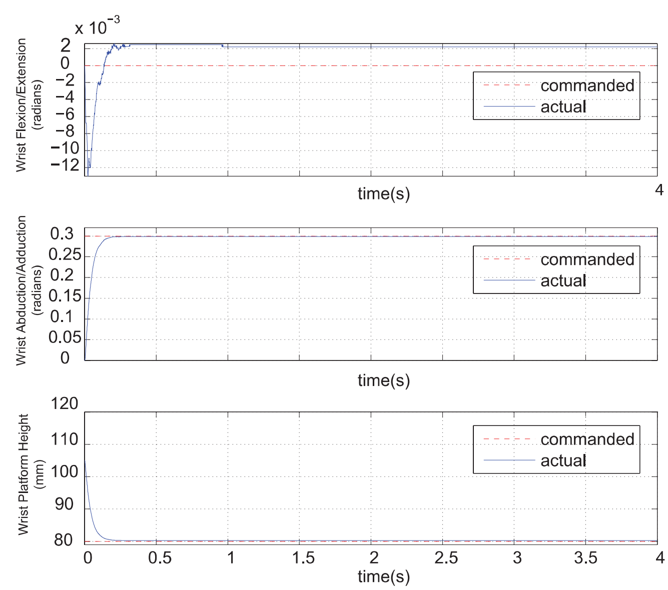

Fig. 17. Set point control of wrist abduction/adduction using inverse kinematics and joint-level PD control (height: 80 mm; abduction/adduction: 0.3 rad; flexion/extension: 0.3 rad). Note the fast response time (< 0.5 s) and small steady-state error.

ther demonstrate that little coupling exists between the various joint axes and that independent joint-level controllers suffice for joint space position control of the device. Also note that the wrist actuators have high bandwidth and a response time of less than half a second. This is evident from the step response and performance during trajectory following.

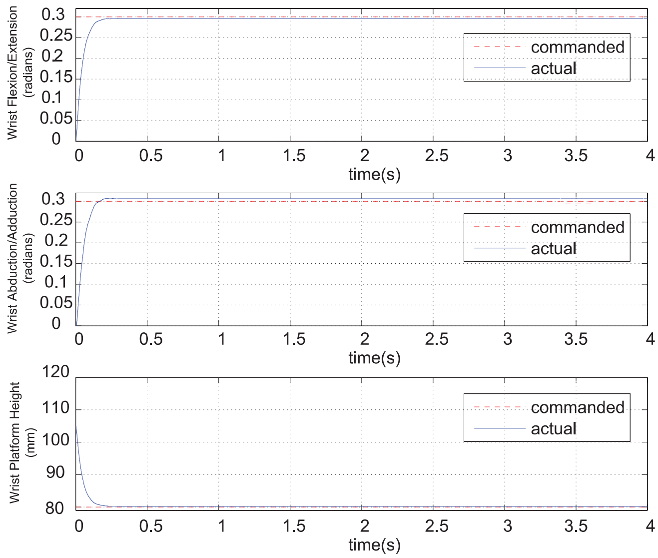

Fig. 18. Set point control of wrist platform using inverse kinematics and joint-level PD control (height: 80 mm; abduction/adduction: 0 rad; flexion/extension: 0.3 rad). Note the fast response time (< 0.5 s) and small steady-state error. The set-point control behavior demonstrates the accuracy of the inverse kinematics computations and low structural coupling between the task-space variables.

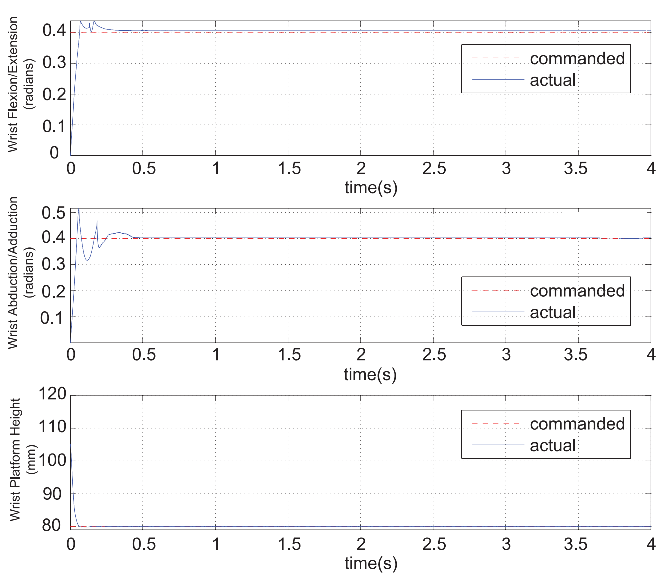

Fig. 19. Step responses for the set point task space controller (amplitude: height: 80 mm; abduction/adduction: 0.4 rad; flexion/extension: 0.4 rad). Note that the system reaches steady state in < 0.5 s and that the overshoot is limited to 1 rad in wrist orientation. This demonstrates the high bandwidth of the device and its capability to simulate stiff contacts.

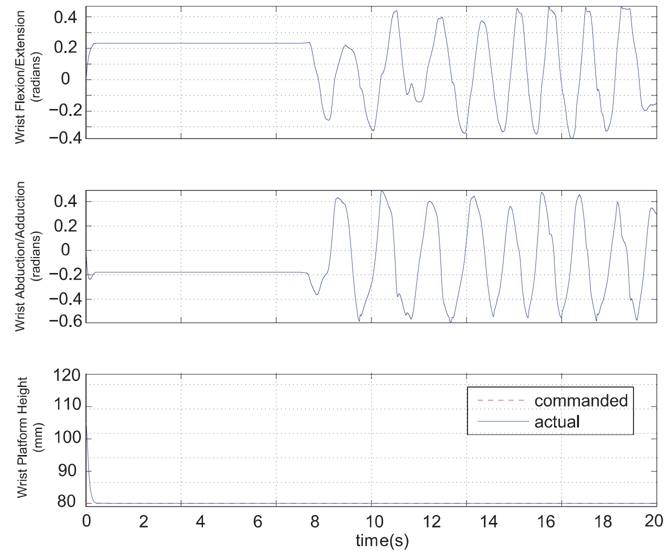

Fig. 20. Free motion of the wrist platform in flexion/extension and abduction/adduction with height constrained. This demonstrates the ability of the device to reproduce natural human movements even when the subject's forearm constrains the platform height.

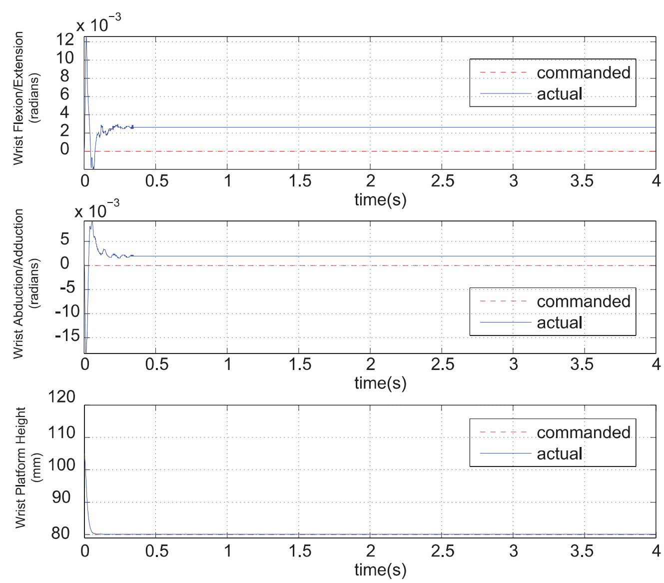

Fig. 21. Task space set-point control of the wrist platform height (height: 80 mm; abduction/adduction: 0 rad; flexion/extension: 0 rad).

As a further verification of the mechanical design and inverse kinematics computations, a set point controller in task-space was implemented. Link lengths corresponding to a de-

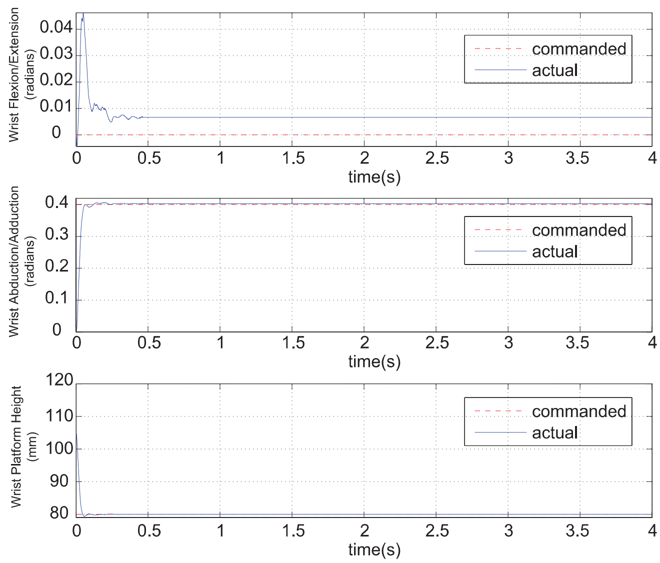

Fig. 22. Task space set-point control of the wrist flexion/extension (height: 80 mm; abduction/adduction: 0 rad; flexion/extension: 0.4 rad).

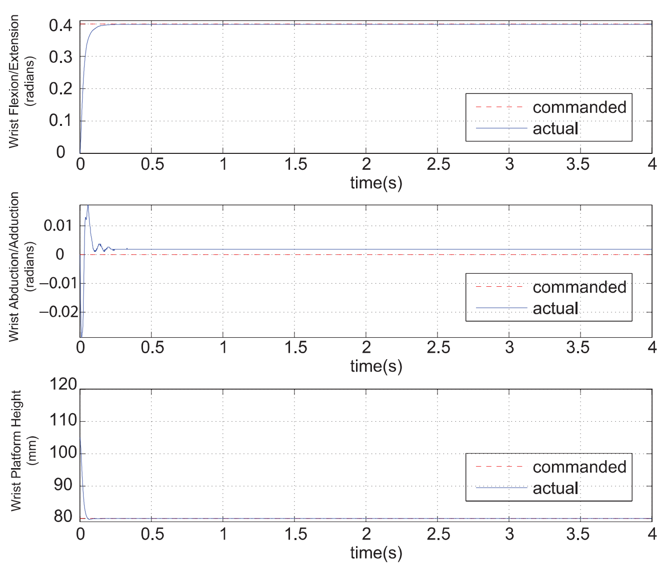

Fig. 23. Task space set-point control of the wrist abduction/adduction (height: 80 mm; abduction/adduction: 0.4 rad; flexion/extension: 0 rad).

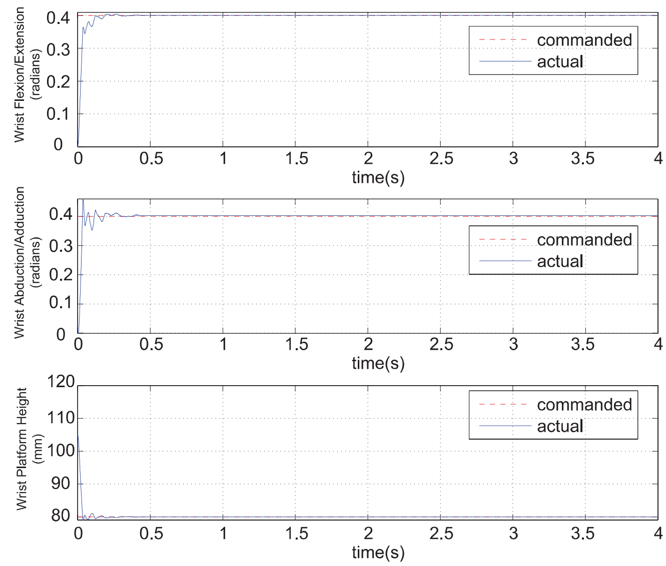

Fig. 24. Task space set-point control of the wrist platform (height: 80 mm; abduction/adduction: 0.3 rad; flexion/extension: 0.3 rad).

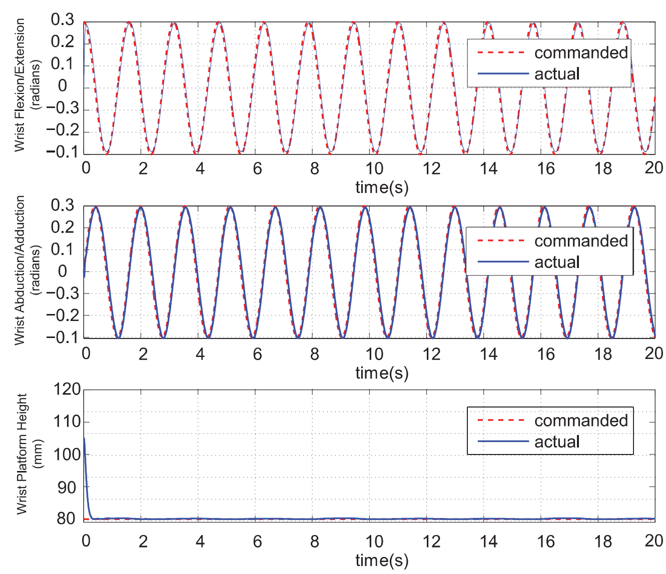

Fig. 25. Task space trajectory tracking control of the wrist platform (height: 80 mm; abduction/adduction and flexion/extension sinusoids of amplitude 1.5 rad at 4 rad s^{-1}).

sired platform position and orientation of the wrist platform were computed using inverse kinematics. These link lengths were then used as a reference signal to the joint-level PD controller. Figures 15–18 show the results for various cases of task-space set point control. Note that in order to change the orientation of the top wrist plate, it was necessary to constrain the height of the platform, as shown in Figures 16 and 17. These results show that the three degrees-of-freedom of the platform are independently or simultaneously controlled with high accuracy demonstrating low structural coupling. Furthermore, note that all parameters reach their steady-state value in less than half a second.

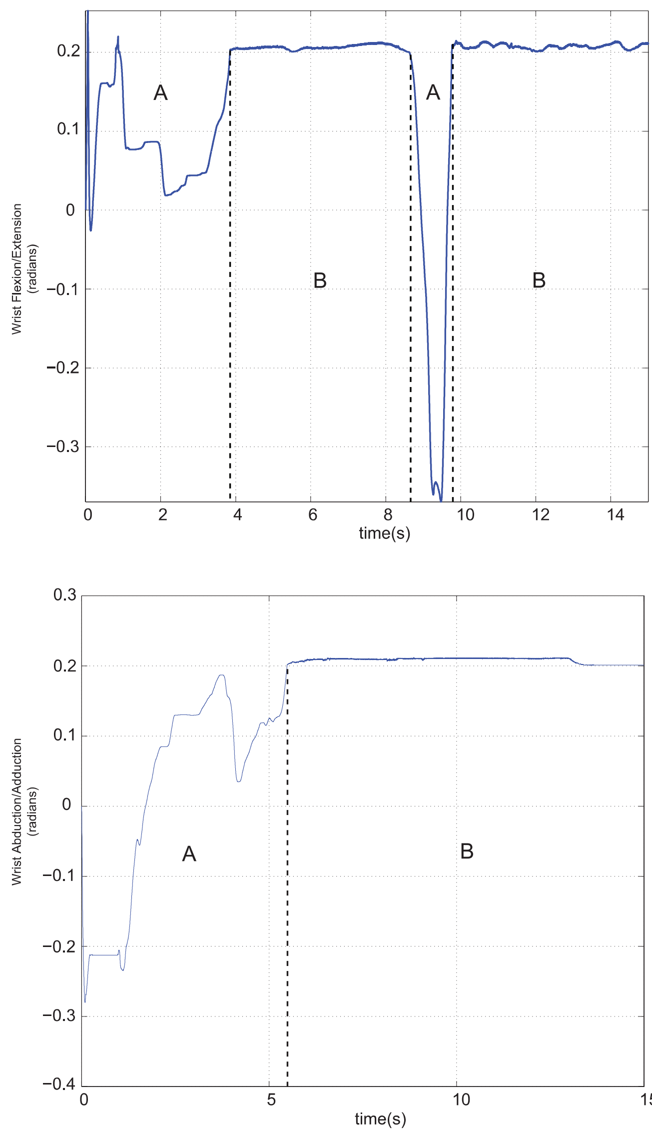

Fig. 26. User interaction with a virtual wall implementation for the wrist platform. A virtual wall located at (a) 0.2 rad wrist flexion/extension and (b) at 0.2 rad wrist abduction/adduction. Regions A and B demonstrate free motion and steady contact with the wall, respectively.

Task Space Position Control. A task space PD controller for the wrist platform was implemented as described in Section 3.2. Figure 19 shows the step responses of the task space PD position controller for the wrist platform to input signals of amplitudes 0.4 rad, 0.4 rad and 80 mm in flexion/extension, abduction/adduction and platform height, respectively. Note that the step response shows the performance of individually controlled degrees of freedom, with others free. The wrist has a fast response (achieves steady state in < 0.5 s) with small overshoot (0.5 rad in flexion/extension

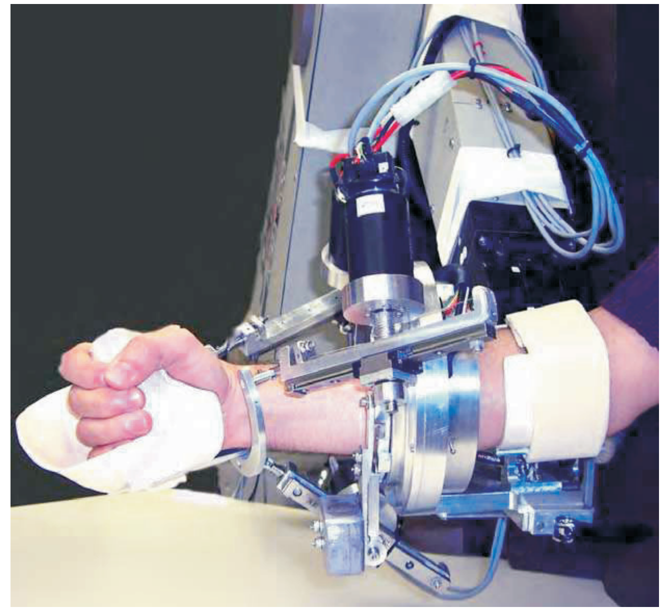

Fig. 27. Subject operating the integrated MIME-*RiceWrist* System.

and 0.1 rad in abduction/adduction) and little oscillations for wrist flexion/extension and abduction/adduction (the system still reaches steady state in approximately 0.5 s). There is a small steady-state error ($< 1\%$), which could be due to cable drive stiffness, friction or modeling errors introduced through the computation of the inverse and forward kinematics and the Jacobian.

Figure 20 shows the wrist platform constrained to a fixed height. During operation, the length of the human forearm constrains wrist platform height. Therefore, it is critical that movement within the human wrist workspace remains unconstrained with the height of the platform maintained constant. As seen in the Figure 20 the task space controller successfully constrains the height without affecting movement in abduction/adduction or flexion/extension.

The four set point control plots, Figures 21–24, show that the three degrees-of-freedom of the platform in the task-space can be controlled independently or simultaneously. This demonstrates that there is little structural coupling between these degrees of freedom. The negligible structural coupling between different degrees-of-freedom of the wrist, low steady-state errors ($< 1\%$), low overshoot (0.01 rad in wrist orientation) and high bandwidth (steady state achieved in < 0.5 s) during task-space PD control with the use of a theoretically computed Jacobian are further proofs of the high quality of mechanical design, manufacturing and assembly. Note that the platform height was constrained when testing step responses in abduction/adduction and flexion/extension as we start at the boundary of the workspace where it is not possible to change

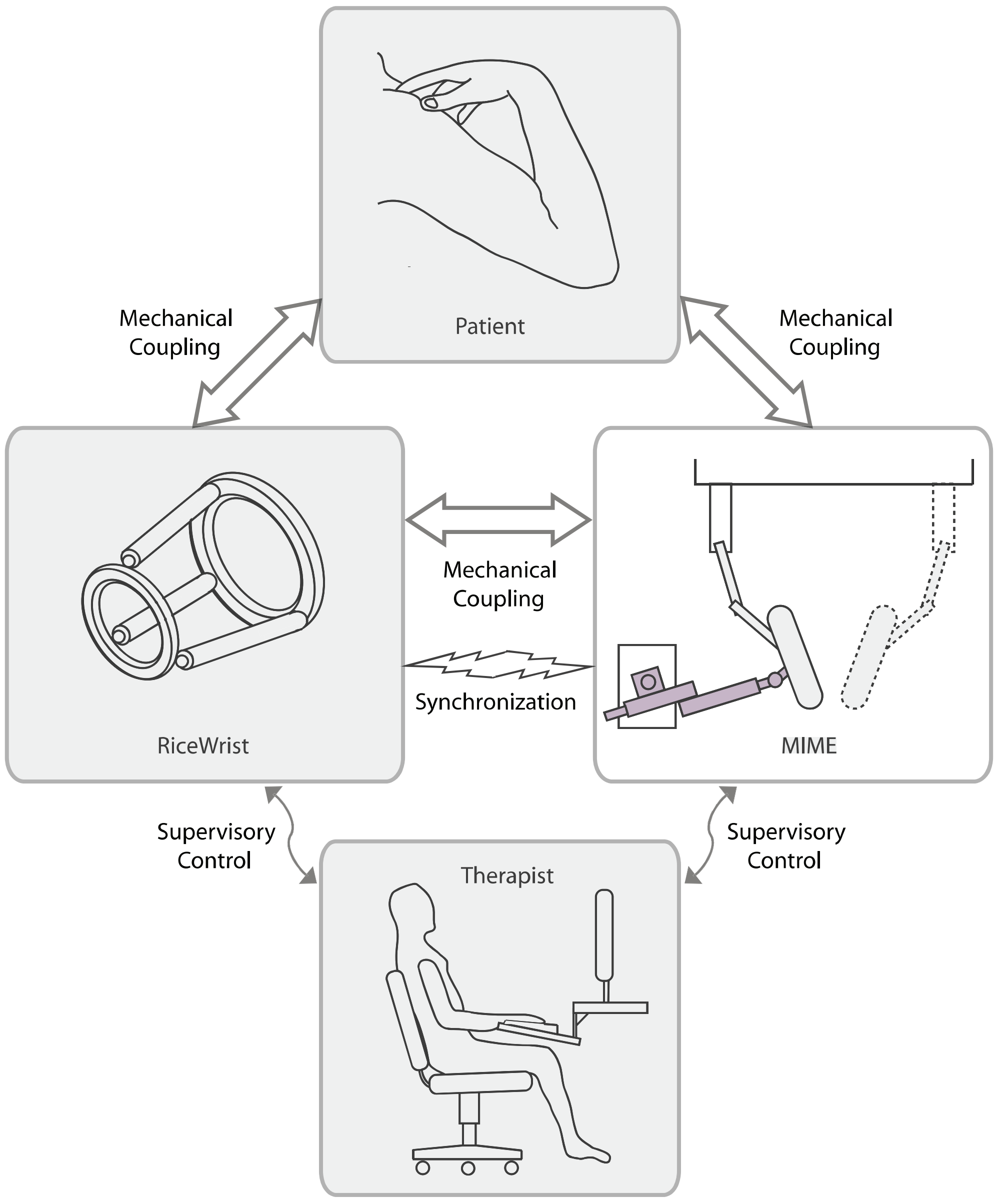

Fig. 28. MIME–*RiceWrist* rehabilitation system setup. The therapist has a supervisory control over the entire therapy session and selects the associated parameters.

orientation of the top plate of the platform without changing platform height.

Finally, the trajectory following behavior of the controller tracking sinusoidal trajectories in abduction/adduction and flexion/extension at 4 rad s^{-1} is shown in Figure 25. Note the quick system response with little overshoot when tracking sinusoidal trajectories of amplitude 0.15 rad at a frequency of 4 rad s^{-1}. Platform height was constrained to 80 mm to simulate operation with a fixed length human forearm. Trajectory following capability is useful for guidance during training or rehabilitation. These results also serve to verify adequate system performance throughout the workspace of the wrist.

Force Control. As described in Section 3.3 force control for the wrist abduction/adduction and flexion/extension was implemented through an impedance controller. Figure 26 depicts a typical user interaction with two virtual walls located at a rotation of 0.2 rad in flexion/extension and abduction/adduction respectively. The virtual wall was implemented as a springdamper system. Although slight chattering is noticed upon contact, the device successfully constrains the operator. Upon decreasing the wall gain, it is noted that chatter occurs at larger user penetration depths into the wall. The platform torque output does not match the limits of the human joints and hence the human operator can saturate the motor output. We believe this actuator saturation along with the low stiffness of the cable drive transmission to be responsible for the chatter.

5. Concluding Remarks

RiceWrist, a four degree-of-freedom haptic wrist exoskeleton robot for rehabilitation and training, has been presented. The device is compact, low-friction and backlash-free, with high manipulability in the workspace of interest. The device allows unconstrained human arm movements over a large workspace and provides for easy measurement of forearm and wrist joint angles. The device exhibits excellent behavior under position control with a fast response time, very small oscillations, little overshoot and small steady-state errors. Furthermore, there is little structural coupling between the controlled degrees-of-freedom of the device: forearm rotation, wrist flexion/extension and wrist abduction/adduction. The ability of the device to independently provide accurate guidance or kinesthetic feedback to individual human joints is critical during motor learning. It is demonstrated that the device is able to simulate sufficiently stiff virtual surfaces, although the quality of the surface is limited by maximum torque output of the robot.

The *RiceWrist* has been integrated with the Mirror-Image Motion Enabler (MIME) Burgar et al. 2000 system (see Figure 27), which provides post-stroke physical therapy for the shoulder and elbow using assisted reaching movements. The *RiceWrist* extends the three unilateral operation modes of MIME to include forearm supination and pronation, wrist flexion and extension, and radial and ulnar deviation. These three unilateral modes of MIME are (see Extension 1) as follows.

- Passive mode: the robot guides the user to a predetermined goal position.
- Active-assisted mode: similar to passive mode, but the robotic assistance does not begin until the patient overcomes some preset force threshold.
- Constrained mode: the patient moves his/her arm against a viscous field to a goal position. A moving virtual wall prevents the patients from retracting their arm.

The passive and active-assistance modes on the *RiceWrist* are implemented using joint-level PD control, whereas the constrained mode is implemented through an impedance controller. Details of the integration of *RiceWrist* with MIME to develop a whole arm rehabilitation setup are provided by O'Malley et al. (2006).

Figure 28 shows the overall setup for the MIME-*RiceWrist* rehabilitation system. The therapist maintains high level supervisory control over the therapy session and customizes the sessions according to the needs of individual patients. Currently, preliminary trials with stroke patients are underway in order to tune the experimental protocols.

Future work with the *RiceWrist* includes further development of the *RiceWrist*–MIME system and clinical trials to study the efficacy of the approach in forearm/wrist rehabilitation. The device will also be used as a test bed for studying mechanisms of human motor learning and development of training methodologies. Further improvements in transmission design to improve the torque output of the device will also be considered.

Acknowledgements

This work is partly supported by contract V674P-3804 from the Central Texas Veterans Health Care System (CTVHCS) in Temple, Texas. The authors would like to acknowledge Joel Huegel and Ryder Winck for their assistance with hardware setup and fabrication. Additionally, we acknowledge Jeanette Richards, OTD, for her clinical input on design specifications for the *RiceWrist*.

Appendix A: Index to Multimedia Extensions

The multimedia extension page is found at http://www.ijrr.org

Table of Multimedia Extensions

Extension	Type	Description
1	video	Modes of the MIME-RiceWrist Rehabilitation Setup

References

Basdogan, C., Ho, C.-H., and Srinivasan, M. A. (2001, Sep). Virtual Environments for Medical Training: Graphical and Haptic Simulation of Laproscopic Common Bile Duct Exploration. **6**(3): 269–285.

Burgar, C. G., Lum, P., Shor, P. C., and Van der Loos, H. F. M. (2000). Development of Robots for Rehabilitation Therapy: The Palo Alto VA/Stanford Experience. *Journal of Rehabilitation Research and Development,* **37**(6): 663–673.

Carignan, C. R. and Akin, D. L. (2003, April). Using Robots for Astronaut Training. In *IEEE Control Systems Magazine*, Volume 23, pp. 46–59.

Charles, S. K., Krebs, H. I., Volpe, B. T., Lynch, D., and Hogan, N. (2005). Wrist Rehabilitation Following Stroke: Initial Clinical Results. In *International Conference on Rehabilitation Robotics*, pp. 13–16.

Dirette, D. and Hinojosa, J. (1994). Effects of Continuous Passive Motion on the Edematous Hands of Two Persons with Flaccid Hemiplegia. *American Journal of Occupational Therapy,* **48**(5): 403–409.

Erlandson, R. F. (1992). Applications of Robotic/Mechatronic Systems in Special Education, Rehabilitation Therapy. *IEEE Transactions on Rehabilition Engineering,* **3**(1): 22–34.

Fasoli, S., Krebs, H. I., Stein, J., Frontera, W. R., and Hogan, N. (2003). Effects of robotic therapy on motor impairment and recovery in chronic stroke. *Archives of Physical Medicine and Rehabilitation,* **84**: 477–482.

Fasoli, S. E., Krebs, H. I., and Hogan, N. (2004). Robotic Technology and Stroke Rehabilitation. *Topics in Stroke Rehabilitation,* **11**: 11–19.

Feygin, D., Keehner, M., and Tendick, R. (2002, March). Haptic Guidance: Experimental Evaluation of a Haptic Training Method for a Perceptual Motor Skill. In *International Symposium on Haptic Interfaces for Virtual Environment and Teleoperator Systems*, pp. 40–47.

Goodall, R. M., Pratt, D. J., Rogers, C. T., and Murray-Leslie, C. M. (1987). Enhancing Postural Stability in Hemi-Plegics Using Externally Applied Forces. *International Journal of Rehabilitation Research,* **10**(4): 132–140.

Gresham, G. E., Alexander, D., Bishop, D. S., Giuliani, C., Goldberg, G., Holland, A., Kelly-Hayes, M., Linn, R. T., Roth, E. J., Stason, W. B., and Trombly, C. A. (1997). Rehabilitation. *Stroke,* **28**(7): 1522–1526.

Gresham, G. H. (1990, Sep). Past Achievements and New Directions in Stroke Outcome Research. *Stroke,* **21 (9 Suppl)**.

Gupta, A. and O'Malley, M. K. (2006). Design of a haptic arm exoskeleton for training and rehabilitation. *IEEE/ASME Transactions on Mechatronics,* **11**(3): 280–289.

Gupta, A. and O'Malley, M. K. (2007). Robotic Exoskeletons for Upper Extremity Rehabilitation. In Rehabilitations Robotics, Sachi S. Kommu (Ed.) I-Tech Education and Publishing, Vienna, Austria, pp. 371–396.

Hayward, V. and Astley, O. (1996). Performance measures for haptic interfaces. In *Robotics Research: The 7th International Symposium*. Springer Verlag.

Hesse, S., Schulte-Tigges, G., Konrad, M., Bardeleben, A., and Werner, C. (2003). Robot Assisted Arm Trainer for the Passive and Active Practice of Bilateral Forearm and Wrist Movements in Hemiparetic Subjects. *Archives of Physical Medicine and Rehabilitation,* **84**(6): 915–920.

Hogan, N. and Krebs, H. I. (2004). Interactive Robots for Neurorehabilitation. *Restorative Neurology and Neuroscience,* **22**: 349–358.

Jack, D., Boian, R., Merians, A. S., Tremaine, M., Burdea, G. C., Adamovich, S. V., Recce, M., and Poizner, H. (2001, Sep). Virtual Reality Enhanced Stroke Rehabilitation. *IEEE Transactions on Neural Systems and Rehabilitation Engineering,* **9**(3): 308–318.

Khalili, D. and Zomlefer, M. (1988). An Intelligent Robotic System for Rehabilitation of Joints and Estimation of Body Segment Parameters. *IEEE Transactions on Biomedical Engineering,* **35**(2): 138–146.

Lee, K. M. and Shah, D. K. (1988, June). Kinematic Analysis of a Three Degrees-of-Freedom in-Parallel Actuated Manipulator. *IEEE Journal of Robotics and Automation,* **4**(3): 354–360.

O'Malley, M. K., Ro, T., and Levin, H. S. (2006). Assessing and Inducing Neuroplasticity with TMS and Robotics. *Archives of PMR, Special Issue on Neuroplasticity and Neuroimaging in Acquired Brain Injury: Measurements, Concepts, and Applications,* **87**(12): 59–66.

O'Malley, M. K., Sledd, A., Gupta, A., Patoglu, V., Huegel, J., and Burgar, C. (2006, Nov). The RiceWrist: A distal upper extremity rehabilitation robot for stroke therapy. In *ASME International Mechanical Engineering Congress and Exposition*.

Prisco, G. M., Avizzano, C. A., Calcara, M., Ciancio, S., Pinna, S., and Bergamasco, M. (1998, May). A Virtual Environment with Haptic Feedback for the Treatment of Motor Dexterity Disabilities. In *IEEE International Conference on Robotics and Automation*, Volume 4, pp. 3721–3726.

Reinkensmeyer, D. J., Dewald, J. P. A., and Rymer, W. Z. (1996). Robotic Devices for Physical Rehabilitation of Stroke Patients: Fundamental Requirements, Target Therapeutic Techniques, and Preliminary Designs. *Technology and Disability,* **5**: 205–215.

Reinkensmeyer, D. J., Emken, J. L., and Cramer, S. C. (2004). Robotics, Motor Learning and Neurologic Recovery. *Annual Reviews in Biomedical Engineering,* **6**: 497–525.

Reinkensmeyer, D. J., Takahashi, C. D., Timoszyk, W. K., Reinkensmeyer, A. N., and Kahn, L. E. (2000). Design of Robot Assistance for Arm Movement Therapy Following Stroke. *Advanced Robotics,* **14**(7): 625–637.

Riener, R., Nef, T., and Colombo, G. (2005). Robot-Aided Neurorehabilitation of the Upper Extremeties. *Medical and Biological Engineering and Computing,* **43**: 2–10.

Sledd, A. and O'Malley, M. K. (2006). Performance Enhancement of a Haptic Arm Exoskeleton. In *International Symposium on Haptic Interfaces for Virtual Environment and Teleoperator Systems*, pp. 375–381.

Stein, J. (2004). Motor Recovery Strategies after Stroke. *Topics in Stroke Rehabiliation,* **11**: 12– 22.

Sveistrup, H. (2004). Motor Rehabilitation using Virtual Reality. *Journal of NeuroEngineering and Rehabilitation*, **1**(10).

Thom, T., Haase, N., Rosamond, W., Howard, V. J., Rumsfeld, J., Manolio, T., Zheng, Z.-J., Flegal, K., O'Donnell, C., Kittner, S., Lloyd-Jones, D., Goff, Jr, D. C., Hong, Y., Adams, R., Friday, G., Furie, K., Gorelick, P., Kissela, B., Marler, J., Meigs, J., Roger, V., Sidney, S., Sorlie, P., Steinberger, J., Wasserthiel-Smoller, S., Wilson, M., and Wolf, P. (2006). Heart disease and stroke american heart association subcommittee. *Circulation,* **113**: e85–e151.

Todorov, E., Shadmehr, R., and Bizzi, E. (1997). Augmented Feedback Presented in a Virtual Environment Accelerates Learning of a Difficult Motor Task. *Journal of Motor Behavior,* **29**(2): 147–158.

Tsagarakis, N., Caldwell, D. G., and Medrano-Cerda, G. (1999, Sep.). A 7DOF Pneumatic Muscle Actuator Powered Exoskeleton. In *International Workshop on Robot and Human Interaction*, pp. 327–333.

White, C. J., Scneider, A. M., and Brogan Jr., W. K. (1993). Robotic Orthosis for Stroke Patient Rehabilitation. In *IEEE International Conference on Engineering and Medical Biology*, pp. 1272–1273.

Wolf, P. A., D'Agostino, R. B., O'Neal, M. A., Sytkowski, P., Kase, C. S., Belanger, A. J., and Kannel, W. B. (1992). Secular Trends in Stroke Incidence and Mortality: The Framingham Study. *Stroke,* **23**: 1551–1555.

Yoshikawa, T. (1985). Manipulability of Robotic Mechanisms. *International Journal of Robotics Research,* **4**(2): 3–9.